

Novel $|V_{cb}|$ extraction method via boosted bc -tagging with *in-situ* calibration

Yuzhe Zhao,* Congqiao Li,† Antonios Agapitos, Dawei Fu, Leyun Gao, Yajun Mao, and Qiang Li
 School of Physics and State Key Laboratory of Nuclear Physics and Technology, Peking University, 100871 Beijing, China
 (Dated: March 4, 2025)

We present a novel method for measuring $|V_{cb}|$ at the LHC using an advanced boosted-jet tagger to identify “ bc signatures”. By associating boosted $W \rightarrow bc$ signals with bc -matched jets from top-quark decays, we enable an *in-situ* calibration of the tagger. This approach significantly suppressed backgrounds while reducing uncertainties in flavor tagging efficiencies, a key factor in measurement precision. Using simulated datasets equipped with advanced and consistent large and small radius jet tagging models (the so-called **Sophon** and the newly developed **SophonAK4**, which are validated to perform comparably to taggers in ATLAS and CMS), we show that the new method complements the conventional small radius jet approach and outperforms it under the HL-LHC projection. Our work offers a new perspective for the precision $|V_{cb}|$ measurement and highlights the potential of using advanced tagging models to probe unexplored boosted regimes at the LHC.

Introduction.— Precise measurements of $|V_{cb}|$ are essential for understanding the Cabibbo-Kobayashi-Maskawa (CKM) sector of the standard model (SM). Established measurements have only relied on B -meson decay and have achieved an uncertainty of approximately 2% [1, 2]; yet, a persistent tension exists between results from inclusive and exclusive B decay methods (see a review in Ref. [3]). Complementary extraction of $|V_{cb}|$ at the weak scale via W boson decays through $\Gamma(W \rightarrow bc)/\Gamma(W \rightarrow qq')$ [4] provides a new angle to probe $|V_{cb}|$ at the weak scale, and with different conditions of theoretical and experimental uncertainties. Its potential has been explicitly explored in the context of HL-LHC [5] and future Higgs factories [6]. However, the small branching ratio of $W \rightarrow bc$ decays requires high-luminosity data to achieve competitive precision. A key challenge across these studies is controlling the experimental uncertainties from flavor-tagging and mistagging efficiencies [4–6]. Reducing these uncertainties will be valuable to enhancing the unique opportunity to probe $|V_{cb}|$ via $W \rightarrow bc$ decays.

We propose here a novel approach to extract $|V_{cb}|$ in the Lorentz-boosted regime at the LHC to mitigate this issue. This method offers two key advantages. First, boosted bc -tagging will enable significantly stronger suppression of background processes. This is similar to the recent advancements at the LHC, where increasingly sophisticated deep learning techniques for boosted bb - and cc -tagging have brought substantial improvements in measurements related to $H \rightarrow bb/cc$ decays [7–10]. Second, a novel opportunity for employing bc -tagging is its ability to facilitate *in-situ* calibration of the signal process, bypassing the need for calibration on a proxy phase space that typically introduces large uncertainties in tagging efficiencies as in bb and cc cases [11, 12]. This is because, in the semi-leptonic $t\bar{t}$ phase space, hadronic top decays produce a distinct signature where a b quark

from t decay and a c quark from W decay form one large- R jet. With a stringent bc -tagging selection, the background is almost entirely dominated by “ bc -matched” jets. Thus, the bc -tagger efficiency for the signal process can be corrected using a shared unconstrained scale factor derived from the above mentioned “ bc -matched” background region. This not only reduces uncertainty in boosted-jet bc -tagging efficiency but also mitigates the dependence of remaining event selections on b/c flavor tagging, thereby enabling more precise extraction of $|V_{cb}|$ under high-luminosity conditions. Figure 1 highlights the key features of our proposed method.

We conduct in-depth experiments to demonstrate these advantages in this study. We follow the spirit to design synchronized strategies that enable a direct comparison between our novel boosted-channel approach with the established resolved-channel method, which only utilizes small- R jet tagging (as in Refs. [4, 13]). To benchmark the advancements achieved in ATLAS and CMS’s flavor tagging performance on large- and small- R jets, we employ advanced deep learning models for tagging on

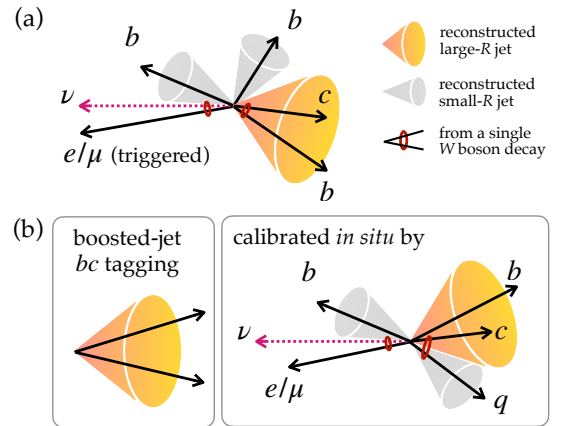


FIG. 1. Illustration of (a) the boosted event topology of semi-leptonic $t\bar{t}$ channel including a $W \rightarrow bc$ decay, and (b) techniques of boosted-jet bc tagging and *in-situ* calibration introduced in this work.

* yuzhe.zhao@cern.ch

† congqiao.li@cern.ch

Delphes simulation, the Sophon model [14] and the newly developed SophonAK4, which are validated to produce realistic performance as in actual experiments. Specifically, the Sophon model is used to tag the resonance bc signatures in the boosted regime. Our synchronized strategies involve aligning the flavor tagger developments for large- and small- R jets (via Sophon and SophonAK4), applying consistent multivariate techniques for event-level signal-background discrimination, and performing a unified counting analysis to extract $|V_{cb}|$ and evaluate the impact of flavor-tagging-related uncertainties. In the HL-LHC projection, our results demonstrate that the uncertainty in $|V_{cb}|$ can be reduced by 30% compared to the conventional approach, assuming consistent tagging performance benchmarks. To conclude, we analyze the underlying reasons for these improvements and discuss the broader implications of this novel method.

Flavor tagging models.— Boosted bc -tagging has not been tested in actual LHC experiments but was covered in the recent Sophon model proposed by some of the authors—a next-generation large- R jet tagger designed for optimal performance across all possible boosted-jet final states [14]. It is essential to verify that the bc -tagging performance demonstrated by Sophon aligns with what is achievable in actual experimental conditions. Therefore, we compare resonance bb - and cc -tagging results against state-of-the-art CMS taggers [15, 16] under consistency in signal and background definitions, jet selections, and discriminant definitions. Figure 2 benchmarks the performance of bb , bc , and cc tagging, in terms of the receiver operating characteristic (ROC) curves and the area under the curve (AUC), with signal jets initiated from hypothetical spin-0 $X^{0,\pm} \rightarrow bb/bc/cc$ decay processes with $m_X = 125$ GeV. As expected, bc tagging achieves an AUC between those of bb and cc tagging; at a tight working point, bc -tagging provides stronger QCD jet suppression compared to bb and cc , as QCD processes do not produce bc from gluon splitting. Additionally, bb - and cc -tagging results are found compatible with CMS’s state-of-the-art taggers based on graph neural networks (ParticleNet-MD) and transformers (GloParT). See details for this comparison in Appendix A.

For conventional b and c taggers on small- R jets, we develop the SophonAK4 model in this work to synchronize the tagging techniques with Sophon. The model is trained on anti- k_T small- R jets ($R = 0.4$) [17] simulated with MG5_aMC@NLO v2.9.18 [18] for event matrix-element generation, Pythia 8.3 [19] for hadronization, and Delphes 3.5 [20] for fast detector simulation and object reconstruction, following the JetClass-II dataset configurations [14]. SophonAK4 achieves b - and c -tagging performance compatible to ATLAS and CMS. Its b -tagging performance is slightly inferior to the widely-adopted DL1r tagger in ATLAS [21] and DeepJet in CMS [22], and c -tagging performance falls between DeepJet and ParticleNet in CMS [23, 24]. For choosing b - and c -tagging working points, we follow the recent ATLAS strategy for DL1r [25], defining five exclusive regions—B1,

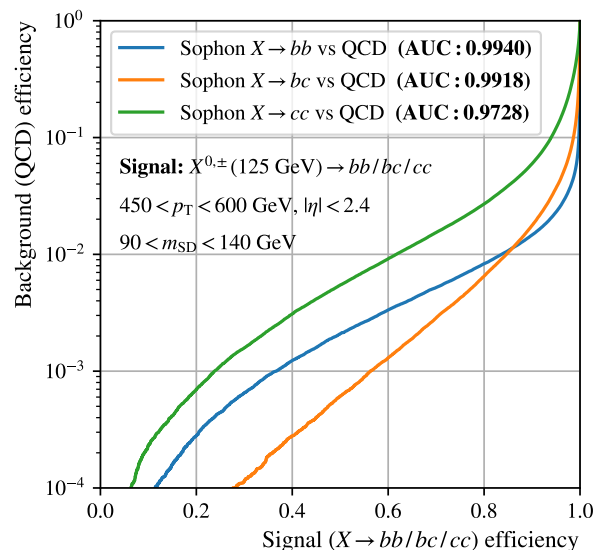


FIG. 2. Performance of the Sophon model on bb , bc and cc tagging, shown as receiver operating characteristic (ROC) curves for signal jets versus the background QCD jets, with area under the curve (AUC) values annotated. Signal jets originate from resonant spin-0 $X^{0,\pm} \rightarrow bb/bc/cc$ decays with $m_X = 125$ GeV. The bb - and cc -tagging performance is consistent with CMS’s state-of-the-art taggers [15, 16] under the same phase-space selection.

B2 for b -tagged, C1, C2 for c -tagged, and N for non-tagged regions—to facilitate simultaneous b - and c -jet identification and enable reasonable estimation of flavor-tagging uncertainties introduced below. Details on SophonAK4 training, validation, and tagging region definitions are provided in Appendix B.

Experimental setup.— Our experiment is conducted on simulated datasets for the LHC pp collision at $\sqrt{s} = 13$ TeV. We study the phase space triggered by a single isolated electron or muon. Thus, events are mainly dominated by the top quark-antiquark pair production ($t\bar{t}$) process, with contributions from other SM processes. The simulated processes include W +jets with leptonic W decay, and $t\bar{t}$, single top in association with a W boson (tW) and diboson WW production in their semi-leptonic decay channel. Events are generated with MG5_aMC@NLO v2.9.18 at the leading order (LO), with additional parton emissions matched to parton showers [26], and decays of t and W implemented at the matrix-element level. The simulation employs SM values for m_t , m_W , and CKM matrix elements. The inclusive cross section of each process are scaled to their higher-order calculations [27–30]. Parton showers are modeled with Pythia 8.3 [19] with NNPDF 3.1 next-to-next-to-LO (NNLO) parton distribution function (PDF) set [31].

The detector simulation is performed using Delphes 3.5 with the same configuration card as JetClass-II. It is based on the default CMS simulation card with modifications to (1) account for track smearing according to CMS tracker resolution, to enable realistic

flavor tagging performance via **Sophon** and **SophonAK4** on **Delphes** simulation, and (2) include pileup (PU) effects with an average of 50 PU vertices, and apply PU mitigation through the PU per particle identification (PUPPI) algorithm [32]. The energy-flow (E-flow) objects modified by PUPPI are clustered into small- and large- R anti- k_T jets with $R = 0.4$ and $R = 0.8$, using minimum p_T thresholds of 25 and 200 GeV, respectively. These procedures ensure consistency with algorithms used in CMS to mitigate PU and reconstruct jets.

The single-lepton trigger criteria are imposed, requiring a reconstructed electron with transverse momentum $p_T > 24$ GeV or a muon with $p_T > 32$ GeV, along with pseudorapidity and isolation constraints. After trigger selection, the estimated event yields at an integrated luminosity of 140 fb^{-1} are 2.5×10^9 , 1.8×10^7 , 2.2×10^6 , and 3.2×10^6 for W +jets with leptonic W decay, $t\bar{t}$, tW , and WW processes, respectively. The signal consists of the latter three processes with $W \rightarrow bc$ decays, yielding 1.8×10^4 events in total under the same luminosity.

Analysis strategies.— We begin by describing the analysis strategy for the boosted regime. In this context, events must contain at least one large- R jet that is isolated from the trigger lepton, satisfying $\Delta R(\text{jet}, \text{lepton}) > 0.8$. The jet with the highest p_T is designated as the W candidate jet (W_{cand}) and is required to have a soft-drop mass [33, 34] within 60–110 GeV. Due to the topology of boosted events, only about 6% of signal events survive this preselection. As illustrated by Fig. 1, the W_{cand} jet can originate from the hadronic decay of a single W or a top quark, containing all or part of their final-state products, or from QCD radiations. To differentiate these origins, t/W -initiated jets are categorized into five classes based on whether each daughter quark of t/W is matched to the W_{cand} jet within $\Delta R(\text{jet}, \text{quark}) < 0.8$. An additional category is defined for jets originating from QCD radiation. The six categories and their corresponding proportions are: top(bqq')-matched (0.7%), top(bc)-matched (3.1%), top(bq)-matched (where q is not a c) (12.3%), $W(qq')$ -matched (23.3%), non-matched (14.7%), and QCD-originated (45.9%).

The boosted-regime method follows a two-stage strategy. First, a stringent selection is applied to the **Sophon** discriminant to enhance the bc content purity. Following the principle from Ref. [14], the discriminant is defined as

$$D_{bc} = \frac{g_{X \rightarrow bc}}{g_{X \rightarrow bc} + g_{X \rightarrow bq} + g_{X \rightarrow cs} + g_{X \rightarrow bqq} + g_{\text{QCD}}} \quad (1)$$

from **Sophon**'s 188 output scores \vec{g} . This formulation ensures that all background contributions are effectively suppressed. In the second stage, a multivariate classifier is used to optimally distinguish W_{cand} jets associated with $W(qq')$ -matched signatures from other cases, without utilizing the **Sophon** tagging information. For this, we adopt an efficient deep learning approach: training a particle-transformer network [35] to classify events into the following categories:

$W(qq')$ -matched, “top(bc)+top(bq)”-matched, top(bqq')-matched, non-matched cases, and W +jets background, using event-object-level features. The input objects with their features include:

- The triggered lepton, with its 4-vector;
- Missing transverse momentum p_T^{miss} , with its constructed 4-vector assuming $\eta, m = 0$;
- The W_{cand} large- R jet, with its 4-vector;
- Up to five small- R jets exclusive to the triggered lepton and W_{cand} , with their 4-vectors and flavor-tagging labels, indicating the **SophonAK4**-tagged region (B1, B2, C1, C2 and N) they belong to.

This deep learning algorithm efficiently combines kinematics properties, such as the invariant mass and ΔR of all possible object pairs, achieving superior classification performance [35]. Figure 3 (left and middle) shows the classifier output distribution for background events, categorized by their truth-matching criteria, and the signal process, both before and after the **Sophon** D_{bc} selection. Notice that after a stringent **Sophon** D_{bc} selection, the background is predominantly composed of the top(bc)-matched component. We note that the spirit in this two-stage method is to use event-level information fully independent of W_{cand} content to construct the classifier to decorrelate the classifier output with D_{bc} . Thus, the D_{bc} tagging efficiency can be calibrated by pairing the bc -matched background with the signal and correcting both yields using a shared, unconstrained scale factor, as will be detailed in the $|V_{cb}|$ extraction.

We then introduce the conventional resolved-regime strategy, similar to that initiated in Ref. [4] while maintaining consistency with the boosted channel. Here, we require each event to have exactly one lepton and at least four small- R jets exclusive to the triggered lepton, with at least three jets tagged as b/c (i.e., labeled as B1, B2, C1, or C2). This selection retains about 28% of triggered signal events. To achieve comparable event classification performance to the boosted regime, we employ a particle-transformer-based classifier to distinguish signal versus background events. The input objects (and features) for this classifier include the trigger lepton (its 4-vector), p_T^{miss} (its constructed 4-vector), and up to six small- R jets exclusive to the triggered lepton (their 4-vectors and five **SophonAK4** tagging labels). The classifier score distribution is shown in Fig. 3 (right), showing the discrimination ability of signal events versus all background processes. Further details on the classifier development for both the boosted and resolved channels can be found in Appendix C.

$|V_{cb}|$ extraction and uncertainty estimates.— For both boosted and resolved channels, we extract $|V_{cb}|$ by performing a counting analysis on events that pass an optimized classifier score threshold. We define the following event counts: N_s as the predicted signal events count, N_{b0} as the predicted count of backgrounds that do

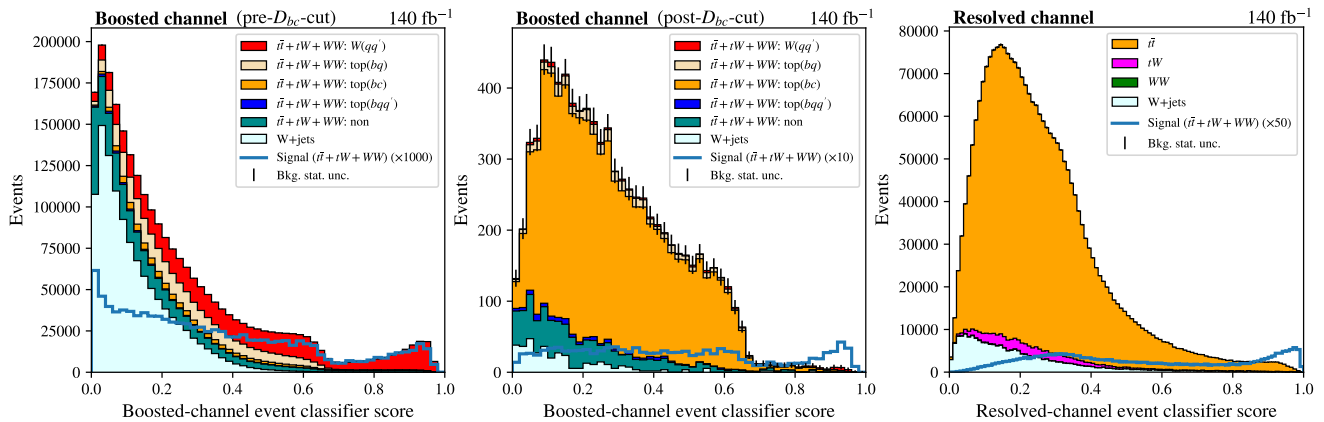


FIG. 3. **Left and middle:** Distributions of the classifier score in the boosted channel before and after the *Sophon* discriminant D_{bc} selection. **Right:** Distribution of the classifier score in the resolved channel. Note that in the boosted channel, the event-level classifiers aim to distinguish the $W(qq')$ -matched jets from the “top(bc)+top(bq)”, top(bqq')-, non-matched cases and W +jets, while in the resolved channel, it is trained against the signal process against W +jets, $t\bar{t}$, tW , and WW , background components, as elaborated in the text.

not contain a hadronically decayed W boson, and N_{b1} as the predicted count of backgrounds involving a hadronically decayed W boson from non- bc sources. The signal strength μ ($= N_s/N_s^{\text{SM}}$) is related to $|V_{cb}|$ by

$$\mu = \left(\frac{|V_{cb}|^{\text{obs}}}{|V_{cb}|^{\text{SM}}} \right)^2, \quad (2)$$

at leading order in α and α_s . Notice that the inclusive hadronic W decay width is proportional to $\sum_{i=u,c; j=d,s,b} |V_{ij}|^2$, which is constant due to CKM unitarity. Thus, the sum $N_s + N_{b1}$ is constrained to be constant, leading to the relation

$$N_{b1} = \frac{1 - \mu r}{1 - r} N_{b1}^{\text{SM}}, \quad (3)$$

$$\text{where } r \equiv \frac{\Gamma(W \rightarrow bc)}{\Gamma(W \rightarrow qq')} = \frac{1}{2} (|V_{cb}|^{\text{SM}})^2, \quad (4)$$

while N_{b0} remains unchanged. The likelihood function is constructed as a Poisson distribution with the mean value of $N_s(\mu) + N_{b1}(\mu) + N_{b0}$, and is modified as follows to incorporate flavor-tagging-related uncertainties.

In both channels, we consider the effect of varying efficiencies for genuine b , c , and light jets tagged or mistagged into five regions (B1, B2, C1, C2 and N), resulting in 15 independent factors affecting $N_{s,b0,b1}$. In ATLAS and CMS, these efficiencies and their uncertainties are measured in dedicated b -, c - and light-flavor-enriched regions [36–40]. We reference the recent ATLAS measurement using the 140 fb^{-1} Run 2 data [25] to acquire these uncertainties: the b - (c -)tagging efficiency uncertainty ranges from 0.01–0.08 (0.04–0.10), and the mistagging rate uncertainty for light jets as b (c -)tagged jets ranges from 0.20–0.25 (0.12–0.13). Detailed values are provided in Appendix B. For each of the 15 sources, we vary the corresponding efficiency up to its $+1\sigma$ value,

normalize the inclusive event yield to remain constant, then evaluate the impact on $N_{s,b0,b1}$. This includes 15 nuisance parameters $\vec{\nu}$ that modify the likelihood by each applying three multiplicative factors to scale $N_{s,b0,b1}$, following log-normal distributions. We show in Fig. 4 the relative increase in the background count due to $+1\sigma$ variations in the 15 sources. The boosted and resolved channels are compared. We notice that in the boosted channel, b -tagging efficiency is a predominant factor, whereas in the resolved channel, multiple factors contribute more significantly to the overall uncertainty. These include both b/c -tagging efficiencies and $c/\text{light} \rightarrow b$ jet mistagging rates. This is because the resolved-channel classifier relies more heavily on identifying multiple b and c jets; in the boosted channel, the $W \rightarrow bc$ tagging is integrated within large- R jet techniques. In addition, the classifier threshold is tighter in the resolved channel to optimize sensitivity. Figure 4 illustrates that the boosted channel is less affected by the small- R jet flavor tagging uncertainties.

In the boosted channel, the large- R jet D_{bc} tagging efficiency is calibrated *in situ* by introducing an unconstrained multiplicative factor λ , which is applied to both the signal and the top(bc)-matched background in the post- D_{bc} -cut region (i.e., the region without applying a cut on the classifier score). This factor introduces an additional Poisson term in the likelihood to constrain the event yield in this region. Thus, μ , $\vec{\nu}$, and λ will be simultaneously extracted in the fit.

Results and discussion.— To summarize the $|V_{cb}|$ measurement results, Fig. 5 presents the total uncertainty in $|V_{cb}|$ for the resolved and boosted channels under different integrated luminosity scenarios, obtained from the best-fit value and uncertainty of μ . In the contexts of Run 2 (140 fb^{-1}), Run 2 and 3 combined (450 fb^{-1}), and the HL-LHC (3000 fb^{-1}), we also pro-

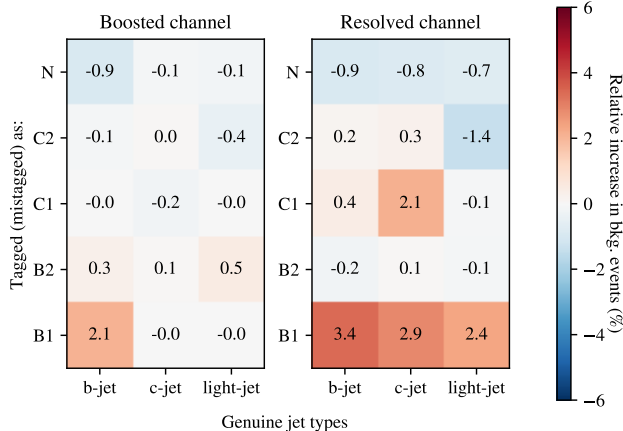


FIG. 4. Comparison of the boosted and resolved channels showing the percentage increase in background events when each of the 15 flavor tagging and mistagging efficiencies is varied to $+\sigma$. These 15 factors correspond to the efficiencies for genuine b , c , and light jets being tagged or mistagged into five categories: B1, B2, C1, C2, and N, as defined by the SophonAK4 scores.

TABLE I. Comparison of the fraction uncertainties of $|V_{cb}|$ contributed by small- R jet flavor tagging (i.e., b/c tagging), large- R jet tagging (i.e., D_{bc} tagging) and statistical errors, for the boosted and resolved channels.

Luminosity (channel)	b/c -tag.	D_{bc} -tag.	stat.
140 fb^{-1} (boosted)	0.036	0.100	0.191
140 fb^{-1} (resolved)	0.065	—	0.154
450 fb^{-1} (boosted)	0.036	0.056	0.106
450 fb^{-1} (resolved)	0.065	—	0.086
3000 fb^{-1} (boosted)	0.035	0.022	0.041
3000 fb^{-1} (resolved)	0.065	—	0.033

vide the uncertainties contributed by b/c tagging and D_{bc} tagging, and statistical errors, as listed in Table I. These uncertainties are obtained by individually freezing \vec{v} and λ in the fit. Here, we assume that the uncertainty in flavor tagging efficiency does not decrease with increasing luminosity, as in the actual experiments, the b/c tagger scale factor measurements are often performed separately for different data-taking conditions [36–40]. Notably, under the 140 fb^{-1} condition, our benchmark predicts an uncertainty for the conventional resolved channel as $\Delta|V_{cb}|/|V_{cb}| = 0.065$ (flavor tag. syst.) \oplus 0.154 (stat.). This is consistent with the preliminary expected result from ATLAS [41] at around 0.13 (syst.) \oplus 0.13 (stat.), thus providing good validation to our flavor tagging benchmark and analysis strategy.

From Fig. 5 and Table I, we observe that the boosted channel is predominantly limited by statistical uncer-

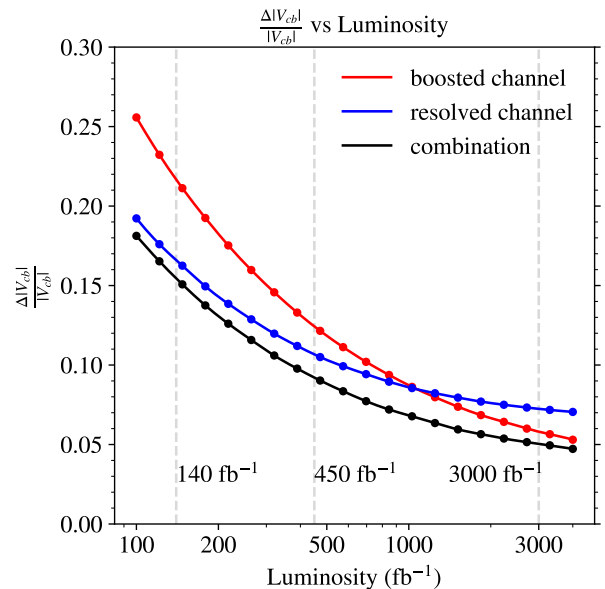


FIG. 5. The total fractional uncertainty of $|V_{cb}|$ obtained from the boosted and resolved channels, as well as their combination, presented under different luminosity conditions. Notably, in the HL-LHC scenario (3000 fb^{-1}), the precision achieved by the boosted channel surpasses that of the resolved channel.

tainty, while the contribution from flavor-tagging-related uncertainty is smaller than that of the resolved channel. As the luminosity increases, the boosted channel demonstrates a significant advantage in the overall uncertainty, surpassing the traditional resolved approach. We attribute this reduced flavor-tagging-related uncertainty to two key factors. First, the use of a novel calibration strategy for the D_{bc} tagger avoids the complexity of finding intricate phase spaces for calibration as in the case of bb - or cc -taggers. Instead, it exploits local *in-situ* constraints for calibration. Second, the decoupling of the event classifier from D_{bc} tagging in the boosted strategy mitigates the classifier’s sensitivity to the change in flavor tagging efficiencies. Consequently, although the boosted regime targets only a small fraction of $W \rightarrow bc$ decays, its better control over uncertainties allows it to outperform the traditional resolved method at the HL-LHC condition.

Given that only around 15% of the events in the resolved channel overlap with those in the boosted channel, a combined measurement can be achieved after excluding these overlapping events from the resolved channel. A simultaneous fit is thus performed, allowing the nuisance parameters to impact both channels. Under the HL-LHC (3000 fb^{-1}) scenario, this combined approach achieves a precision of $\Delta|V_{cb}|/|V_{cb}| = 0.051$, representing a 30% reduction in uncertainty compared to the traditional resolved method. The performance of the combined scenario across different luminosities is also showcased in Fig. 5. Finally, a combination of measurements

from both ATLAS and CMS experiments can further reduce the fraction uncertainty to 0.036, a level of precision sufficient to provide critical insights into resolving the $|V_{cb}|$ puzzle.

Although our study demonstrates the potential of the boosted regime in LHC $|V_{cb}|$ measurement, the precision of the b/c tagging efficiency measurement remains a primary limiting factor. We consider two more optimistic scenarios: one where the uncertainty is reduced by half, and another where the uncertainty scales with luminosity L as $1/\sqrt{L}$. Under these scenarios, the expected improvement in $|V_{cb}|$ precision at 3000 fb^{-1} will reduce, ranging from 0–15%. Besides, we have only considered a limited set of systematic uncertainties. In actual experiments, additional systematic uncertainties arise from experimental sources (e.g., jet energy calibration) and theoretical modeling inaccuracies, which affect both the boosted and resolved regimes. Furthermore, precise control of other background processes is critical. One can rely on multiple control regions to accurately constrain the background contributions.

Conclusion. — In summary, we propose a novel approach for precise $|V_{cb}|$ extraction at the LHC, utilizing the boosted regime. By employing an advanced boosted-jet bc -tagger via the Sophon model and an innovative *in-situ* calibration technique, we factorize the complex requirements for event-level b/c tagging and global calibration into two components: an integrated bc tagging and calibration, and a residual component that is less sensitive to uncertainties in b/c tagging and mistagging efficiencies. This effectively mitigates the impact of uncertainties related to flavor tagging, achieving a generally improved precision over the conventional method.

From a broader sense, recent advancements in deep learning algorithms for particle physics have enhanced sensitivity through well-established boosted channels such as bb and cc , revealing potential in exploring a broader range of boosted final states. This highlights the Sophon philosophy: extending boosted-jet techniques to previously unexplored regions. Hence, this work not only demonstrates an application in a novel boosted phase space beyond established bb and cc contexts but also suggests a more important role for boosted-regime searches in future LHC explorations. As benchmark tagging models with consistent performance on Delphes datasets, Sophon and SophonAK4 will enable future investigations into diverse boosted phase spaces.

Acknowledgement. — This work is supported by National Natural Science Foundation of China (NSFC) under Grants No. 12325504, No. 12061141002, and No. 2075004. YZ and CL appreciate helpful discussions with Sitian Qian and Huilin Qu. This research is supported in part by the computational resource operated at the Institute of High Energy Physics (IHEP) of the Chinese Academy of Sciences.

Data availability. — The Sophon model (for large- R jets), JetClass-II dataset, and its corresponding Delphes

configuration initiated in Ref. [14] are publicly available at the following https URLs^{1,2}. The SophonAK4 model will be made publicly available at this URL³.

¹ <https://huggingface.co/jet-universe/sophon>

² <https://huggingface.co/datasets/jet-universe/jetclass2>

³ <https://huggingface.co/jet-universe/sophon-ak4>

Appendix A: Supplementary details on Sophon’s bc -tagging performance

During the training of the **Sophon** model, the bb , bc , and cc jet classes are generated through the decay of a spin-0 resonance X into bb , bc , and cc final states. These jets exhibit a broad distribution in m_{SD} and p_T : $200 < p_T < 2500$ GeV and $20 < m_{SD} < 500$ GeV. For these jets, a ΔR matching condition between the jet and the two daughter quarks is imposed. During training, sampling-based reweighting is performed on the three jet classes and the QCD jets (as background), along with other categories. This involves a two-dimensional reweighting on (m_{SD}, p_T) to ensure consistent distributions, hence reducing the dependence of the tagger response on jet mass and p_T . Notice that the technical details for the bb and cc jets are consistent with the **GloParT** training method within CMS [16], and the definition of the bc jet class is similar to that of bb and cc , which differs only in quark flavor. Therefore, by verifying the consistency of bb and cc tagging with actual experimental results, we can reasonably conclude that the performance of the **Sophon** bc tagger is comparable to that observed in actual experiments.

The performance evaluation of **Sophon** (Fig. 2) is conducted on a 125 GeV resonance $X^{0,\pm}$ decaying into bb , bc , and cc as signal jets. The kinematic properties of the resonance X follow the p_T and η distributions observed in gluon-gluon-fusion Higgs boson production. It is verified that the kinematic distributions of bb , bc , and cc jets are consistent. The event selection requires the presence of a reconstructed large- R jet, with the leading jet chosen as the candidate. The selected jet must satisfy $450 < p_T < 600$, $|\eta| < 2.4$, and a soft-drop mass requirement of $90 < m_{SD} < 140$. These sample settings and kinematic selections are consistent with those used in the experiment. For signal jets, a jet-quark matching condition is also required. The QCD background is obtained from QCD multijet events, where the leading large- R jet is required to satisfy the same kinematic requirements. The definition of the **Sophon** discriminant follows the same convention as **ParticleNet-MD** and **GloParT**. It is defined as

$$\text{discr}(X \rightarrow \text{sig vs QCD}) = \frac{g_{X \rightarrow \text{sig}}}{g_{X \rightarrow \text{sig}} + g_{\text{QCD}}}, \quad \text{where sig} = bb \text{ or } cc. \quad (\text{A1})$$

Table A1 presents the background rejection rate ($= 1/\epsilon_B$) for bb and cc discriminants at signal efficiencies of $\epsilon_S = 60\%$ and 40% , compared with CMS bb/cc taggers: **DeepDoubleX**, **ParticleNet-MD** (read from Ref. [15], Figs. 5–6), and **GloParT** stage-2 (read from Ref. [16], Figs. 11.12–13). The rejection rate of **GloParT** stage-2 is obtained by taking the ratio of the **GloParT-to-ParticleNet-MD** rejection rate from Ref. [16] and applying it to the **ParticleNet-MD** results from Ref. [15] due to a slight difference in their p_T selections. It is observed that for the bb tagger, **Sophon**’s performance is between the CMS taggers **DeepDoubleX** and **ParticleNet-MD**, but closer to the latter. For the cc tagger, **Sophon** shows superior performance, nearly reaching the best results of **GloParT** in CMS. This difference in b/c tagging performance can be attributed to discrepancies in the b and c jets simulation by the **Delphes** JetClass-II card compared to the actual detector response, as well as the absence of auxiliary variables, such as those related to tracks and secondary vertices, which can further enhance b tagging performance. Specifically, the result indicates that b tagging performance may be slightly underestimated, as also reflected in the performance of **SophonAK4** in the following appendix section.

TABLE A1. Comparison of the **Sophon** model with the established CMS taggers, **DeepDoubleX**, **ParticleNet-MD**, and **GloParT** (stage-2), regarding bb and cc tagging performance. The QCD background rejection rate ($1/\epsilon_B$) is shown for bb and cc tagging at fixed signal efficiencies of $\epsilon_S = 60\%$ and 40% . The CMS results are extracted from the ROC curves in Refs. [15, 16], as detailed in the text.

	Delphes simulation	CMS simulation [15, 16]		
	Sophon	DeepDoubleX	ParticleNet-MD	GloParT (stage-2)
$X \rightarrow bb$ vs. QCD, $\epsilon_s = 60\%$	300	200	370	470
$X \rightarrow bb$ vs. QCD, $\epsilon_s = 40\%$	810	580	970	1380
$X \rightarrow cc$ vs. QCD, $\epsilon_s = 60\%$	110	31	76	110
$X \rightarrow cc$ vs. QCD, $\epsilon_s = 40\%$	320	110	260	360

Appendix B: Supplementary details on SophonAK4 development

1. The training of SophonAK4

To generate the training jet samples for **SophonAK4**, we employ the spin-0 resonance process X decaying into multiple two-prong states. This is consistent with the production mechanism used in **Sophon** training for two-prong

large- R jets. Specifically, events are generated using the $pp \rightarrow HH$ process at LO with the MG5_aMC@NLO 2.9.18 generator, utilizing the HEFT model. To control the p_T and mass of the resonant jets, the minimum p_T of the H boson at the hard-scattering level is sampled at 50 logarithmically spaced points between (100, 2500) GeV. The mass of the H boson is uniformly sampled from (15, 500) GeV with an interval of 5 GeV. The decay of the H resonance and parton showering are simulated using Pythia 8.3. The decay modes (with their corresponding branching ratios) are as follows: bb ($\frac{1}{8}$), cc ($\frac{1}{8}$), ss ($\frac{1}{8}$), dd ($\frac{1}{16}$), uu ($\frac{1}{16}$), gg ($\frac{1}{8}$), ee ($\frac{1}{16}$), $\mu\mu$ ($\frac{1}{16}$), $\tau\tau$ ($\frac{1}{4}$).

The simulated events are processed using Delphes 3 with the JetClass-II configuration. As introduced in Ref. [14], this simulation card is adapted from the CMS detector configuration but includes modifications to the impact parameter of charged particles to match the CMS tracker resolution, following the approach used in the JetClass simulation. Additionally, PU effects with an average of 50 PU interactions are incorporated using the CMS detector configuration with PU. To mitigate PU contamination, the PU per-particle identification (PUPPI) algorithm is applied. This implementation is adapted from the CMS Phase-II detector configuration but includes parameter adjustments to match the Phase-I CMS detector conditions. Specifically, PUPPI assigns a probability value between 0 and 1 to each E-flow object, indicating the likelihood that the object originates from the primary interaction. This value is then used to scale the object's four-vector. The processed E-flow objects are clustered into small- R jets using the anti- k_T algorithm with $R = 0.4$.

Based on truth-matching information, each jet is assigned one of the single-prong or two-prong labels, resulting in a total of 23 jet categories:

1. The single-prong labels include $b, \bar{b}, c, \bar{c}, s, \bar{s}, d, \bar{d}, u, \bar{u}, g, e^-, e^+, \mu^-, \mu^+, \tau_h^-, \tau_h^+$. These correspond to cases where the corresponding truth particle (either a parton or a lepton) is matched to the jet within $\Delta R(\text{jet}, \text{particle}) < 0.4$, and the other particle from the same resonance decay is not matched to the jet.
2. The two-prong labels include $b\bar{b}, c\bar{c}, s\bar{s}, d\bar{d}, u\bar{u}$, and gg , corresponding to cases where both particles from the same resonance decay are matched within the jet.

Jets are required to satisfy the kinematic criteria of $15 < p_T < 1000$ GeV and $|\eta| < 5$. In total, 46 M jets are used for training the model.

For each jet, only jet-consistent-level E-flow features are used as input variables. These features include kinematic variables, particle identification variables, and impact parameter features. This approach closely follows the JetClass dataset configuration and is consistent with the training of the Sophon model, except that small- R jets are used in this case.

Similar to Sophon, the SophonAK4 model adopts the Particle Transformer architecture but with a reduced scale: the embedding dimension and the latent space size of the corresponding MLPs are reduced by half compared to the original Sophon model. Specifically, SophonAK4 consists of 6 particle attention blocks and 2 class attention blocks, with an embedding dimension of 64 and 8 attention heads. The initial particle features are embedded using a 3-layer MLP with (64, 256, 64) nodes, while the pairwise particle features are embedded using a 4-layer elementwise MLP with (32, 32, 32, 8) nodes. The GELU activation function is used throughout the model. Overall, the SophonAK4 model includes around 0.55 M parameters.

A sampling-based reweighting strategy is employed on the two-dimensional histogram of (p_T, η) to ensure uniform classification performance across all p_T and η regions. Specifically, training samples are selected into the training pool with predefined probabilities during the on-the-fly data loading process. These probabilities act as reweighting factors, adjusting the two-dimensional histograms bin by bin. The reweighting is designed to produce normalized distributions for specific reweighting classes. These classes are formed by merging the 23 finely classified categories into 9 groups according to their parton or lepton flavors: b, c, s, d, u, g, e, μ , and τ_h .

The model is trained using a batch size of 512 with an initial learning rate of 5×10^{-4} . The full dataset is split into 80% for training and 20% for validation. The training process spans 80 epochs, with each epoch processing 10 M samples. The optimizer and learning rate scheduler are identical to those used in the Sophon model training.

2. Performance of SophonAK4

The performance evaluation of SophonAK4 is conducted on $t\bar{t}$ events from SM processes to facilitate direct comparison with the performance benchmarks from ATLAS and CMS.

We first compare the performance using ROC curves against various CMS taggers. To ensure consistency, we apply the same phase space selection criteria: jets are required to satisfy $p_T > 30$ GeV and $|\eta| < 2.5$. Jets from $t\bar{t}$ events are assigned truth flavor labels as genuine b, c , and light jets using ghost association in Delphes. We define the following b -tagging discriminant to evaluate the performance of b vs. light jets and b vs. c jets:

$$\text{discr}(\text{SophonAK4 } b \text{ tagging}) = g_b + g_{\bar{b}} + g_{b\bar{b}}. \quad (\text{B1})$$

where \vec{g} represents the raw output scores of the model. For c -tagging, we define the following discriminates,

$$\text{discr (SophonAK4 } c \text{ tagging)} = g_c + g_{\bar{c}} + g_{c\bar{c}}, \quad (\text{B2})$$

$$\text{discr (SophonAK4 } c \text{ vs. } b \text{ tagging)} = \frac{g_c + g_{\bar{c}} + g_{c\bar{c}}}{g_c + g_{\bar{c}} + g_{c\bar{c}} + g_b + g_{\bar{b}} + g_{b\bar{b}}} \quad (\text{B3})$$

These are used to evaluate the performance of c vs. light jets and c vs. b jets, respectively, following the conventions typically used by CMS [24].

Figure B1 presents the performance of b vs. light/ c jets and c vs. light/ b jets. Comparing these results with the CMS benchmarks (refer to Ref. [24], Figures 1 and 3 for the $t\bar{t}$ process), we observe that the b vs. light jet performance is slightly inferior to the widely-adopted DeepJet, while the b vs. c and c vs. light/ b jet performances lie between those of DeepJet and ParticleNet. This observation is consistent with the findings in Appendix A regarding the performance of Sophon. Specifically, the Delphes simulation tends to yield weaker b tagging capability but provides a more realistic c tagging performance.

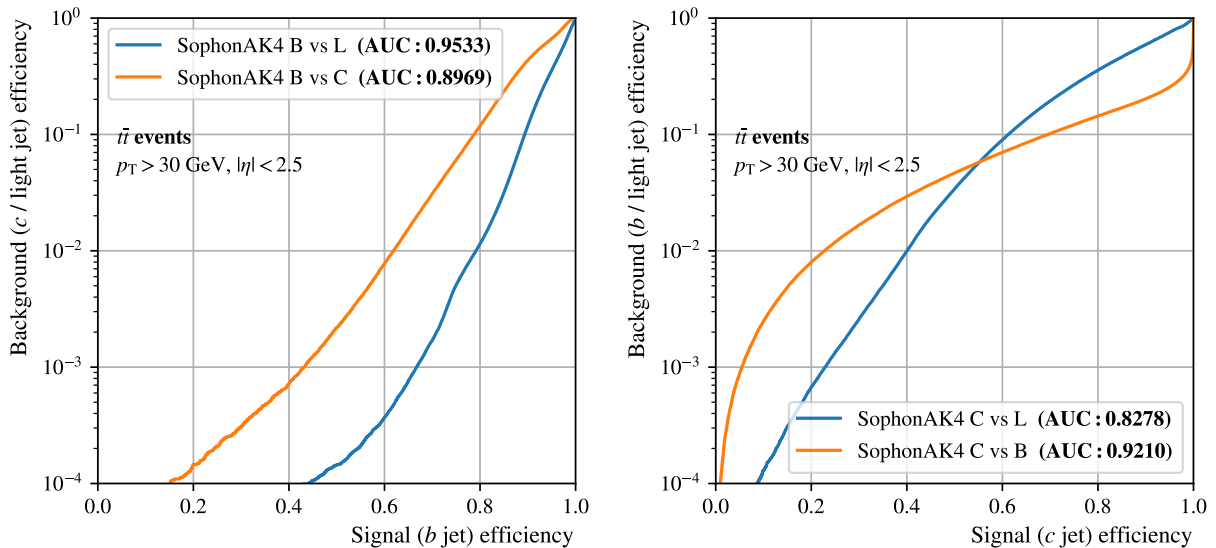


FIG. B1. Performance of the **SophonAK4** model for b versus light/ c jet tagging (left) and c versus light/ b jet tagging, shown as receiver operating characteristic (ROC) curves for signal jets versus the background QCD jets, with area under the curve (AUC) values annotated. The signal and background jets originate from $t\bar{t}$ events and are labeled as genuine b , c , and light jets based on the ghost association criteria. These benchmarks are directly comparable to the performance of the CMS b and c flavor taggers under the same phase-space selection [24], as detailed in the text.

Figure B2 further compares the performance of b vs. light jet tagging across different p_T and η regions for three working points. These working points correspond to b -tagging discriminant thresholds at background efficiencies (ϵ_B) of 10^{-1} , 10^{-2} , and 10^{-3} . By comparing these results with the CMS benchmarks (Ref. [24], Figures 17, 19, 21, 23, 25, 27, 29, and 31), a similar trend is observed: the tagging performance is lower in the low- p_T and high- $|\eta|$ regions but stabilizes at a plateau beyond the turn-on point. This indicates that the **SophonAK4** tagger exhibits realistic flavor tagging behavior across different p_T and η regions.

3. Tagging region definition of SophonAK4

To facilitate simultaneous b and c tagging in this analysis, we adopt the tagging region definition from a recent ATLAS study. Specifically, the tagging regions are defined using the two-dimensional distribution of b -tagging and c -tagging discriminants, resulting in five exclusive regions: B1 and B2 as b -tagged jet enriched regions, C1 and C2 as c -tagged jet enriched regions, and N as the non-tagged region. Each region corresponds to selection efficiencies for genuine b , c , and light jets. The definitions of these regions are based on the tagging region criteria for the widely-adopted DL1r tagger from ATLAS (see Ref. [25], Figure 1). We adopt the same phase space to enable a direct comparison with the ATLAS results, lowering the jet p_T threshold to 20 GeV.

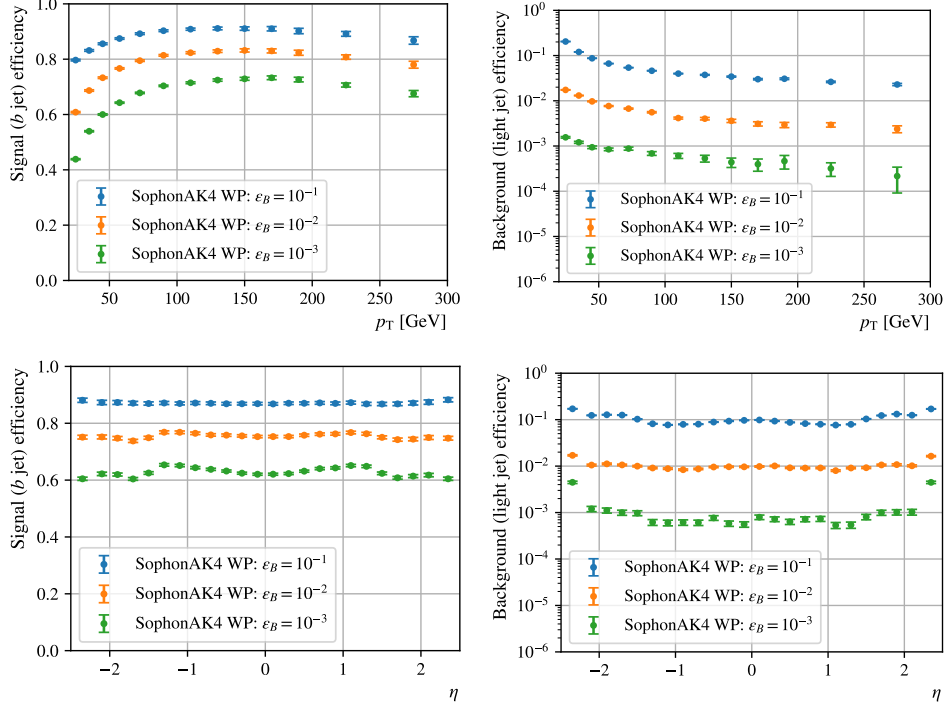


FIG. B2. The b tagging efficiency (left plots) and light-jet mistagging efficiency (right plots) of **SophonAK4** as functions of jet p_T (top plots) and η (bottom plots), evaluated at three different selection working points. These benchmarks are comparable to the performance of the CMS b and c flavor taggers under the same phase-space selection [24], under the three working points: tight, medium, and loose.

Figure B3 illustrates the five tagging regions and the corresponding selection efficiencies for the three jet flavors. Specifically, in regions B1 and B2, the b -jet efficiencies are approximately 60% and 10%; in regions C1 and C2, the c -jet efficiencies are about 25% each.

Comparing the mistag efficiencies with those of the ATLAS DL1r tagger [25], we draw to the following findings:

1. For b vs. light jet tagging, the performance is slightly weaker than DL1r: in the B2 region, the light-jet efficiency is 0.05%, consistent with ATLAS; however, in the B2 region, the light-jet efficiency is 0.21%, which is higher than ATLAS's 0.13%.
2. For b vs. c jet tagging, the performance exceeds that of DL1r: the c -jet efficiencies in the B1 and B2 regions are 0.95% and 2.8%, respectively, which are lower than ATLAS's 2.7% and 5.2%.
3. For c vs. b /light jet tagging, the performance exceeds that of DL1r. In the C1 region, the efficiencies for light and c jets are 0.17% and 2.3%, respectively, compared to ATLAS's 0.9% and 4.8%. A similar trend is observed in the C2 region.

These results demonstrate that the **SophonAK4** tagger achieves competitive and, in some cases, superior performance compared to the DL1r tagger, particularly in distinguishing b from c jets and in c vs b /light jet tagging. Considering the comprehensive comparison of **SophonAK4** tagging performance with the benchmarks from ATLAS and CMS taggers, we conclude that **SophonAK4** serves as a reliable and realistic b/c flavor tagger for **Delphes**-based simulations.

4. Scale factors in tagging efficiencies of **SophonAK4**

To obtain realistic tagging and mistagging efficiency uncertainties based on the five defined tagging regions in this study, we utilize the tagging scale factors derived by ATLAS using 140 fb^{-1} of Run-2 data, corresponding to the five ATLAS's tagging regions [25].

For the case of **SophonAK4**, we assume the scale factor central values to be 1, while the uncertainties are assigned according to the ATLAS results for each flavor's tagging and mistagging efficiencies (collectively denoted as ϵ_{ftag})

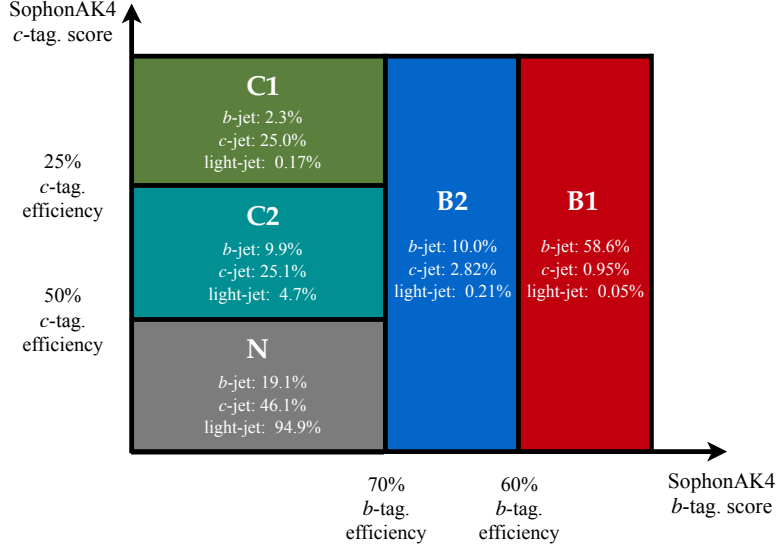


FIG. B3. A schematic of the five flavor tagging regions: B1, B2, C1, C2, and N defined using *SophonAK4* *b*- and *c*-tagging discriminants. The tagging efficiencies annotated for *b*, *c*, and light flavors in these regions are extracted from $t\bar{t}$ events. The region definitions are based on a recent ATLAS study using the DL1r *b*- and *c*-tagging discriminant (see Fig 1 of Ref. [25]).

across the five regions. The scale factors are jet p_T -dependent. By extracting the relevant results from Ref. [25] (Figure 3), we summarize the ϵ_{ftag} uncertainties in Table B1. These uncertainties are incorporated into the $|V_{cb}|$ sensitivity estimation conducted in this work.

TABLE B1. Uncertainties of the scale factors used to correct the *SophonAK4* tagging efficiencies for *b*, *c*, and light flavors in the five regions: B1, B2, C1, C2, and N, binned by jet p_T . These numbers are extracted from the scale factors and their uncertainties derived from the recent ATLAS scale factor measurements for the DL1r flavor tagger (see Auxiliary material, Fig. 3 of Ref. [25]).

jet p_T (GeV)	ϵ_{ftag} uncertainty (<i>b</i> jet)							ϵ_{ftag} uncertainty (<i>c</i> jet)				ϵ_{ftag} uncertainty (light jet)			
	(20, 30)	(30, 40)	(40, 60)	(60, 100)	(100, 175)	(175, 250)	(250, ∞)	(20, 40)	(40, 65)	(65, 140)	(140, ∞)	(20, 50)	(50, 100)	(100, 150)	(150, ∞)
B1	0.07	0.04	0.03	0.01	0.01	0.02	0.03	0.10	0.08	0.08	0.08	0.23	0.22	0.24	0.20
B2	0.07	0.04	0.03	0.02	0.03	0.04	0.08	0.10	0.05	0.05	0.06	0.22	0.22	0.25	0.20
C1	0.06	0.03	0.02	0.02	0.03	0.06	0.14	0.10	0.04	0.04	0.04	0.12	0.12	0.13	0.12
C2	0.05	0.03	0.01	0.01	0.02	0.04	0.10	0.07	0.07	0.06	0.06	0.13	0.13	0.13	0.12
N	0.20	0.12	0.08	0.05	0.07	0.08	0.13	0.07	0.04	0.04	0.04	0.0035	0.0025	0.0025	0.0022

Appendix C: Supplementary details on analysis strategy

This section provides additional details related to the analysis strategy. For both the resolved and boosted channels, the cutflow is summarized in Table C1, following the description provided in the main text. The event yields correspond to those expected for 140fb^{-1} of data. Notice that for the resolved channel, two classifier threshold options are considered. Option B is used in the default analysis, while the other option will be detailed below.

For the classifier training in both the resolved and boosted channels, the input objects, along with their respective features and vectors, are summarized in Table C2. Both classifiers are trained using deep neural networks based on the Particle Transformer (ParT) architecture. The embedded dimension and MLP layer sizes are reduced by half compared to the standard ParT model. The classifiers are trained on specifically simulated SM events, with the event categories described in the main text. Care is taken to ensure that the training and validation samples do not overlap with the inference samples used for event yield estimation. For both channels, the training datasets consist of around 2 M samples. The model is trained using a batch size of 512 and an initial learning rate of 10^{-3} . The dataset is split into 80% for training and 20% for validation. The training process spans 20 epochs, with each epoch processing about 0.5 M samples. The optimizer and learning rate scheduler are consistent with those used in the default ParT model training.

TABLE C1. Cutflow table for boosted and resolved channels. For background processes ($t\bar{t}$, tW and WW) and signal processes, events are further split into five subcategories based on generator-level matching of the W_{cand} large- R jet. Event counts are shown for an integrated luminosity of 140 fb^{-1} .

Selection	$W(l\nu)$ +jets	$t\bar{t}$ (semi-lep.)					tW (semi-lep.)					WW (semi-lep.)		Signal ($t\bar{t} + tW + WW$, w/ $W \rightarrow bc$ decay)								
		total	top(b q')	top(bc)	top(b q)	$W(qq')$ non	total	top(b q')	top(bc)	top(b q)	$W(qq')$ non	total	$W(qq')$ non	total	top(b q')	top(bc)	top(b q)	$W(qq')$ non				
Boosted channel																						
Pass 1 l trigger	250000000	1800000	—	—	—	—	1600000	—	—	—	—	2300000	—	—	18000	—	—	—	—			
+ ≥ 1 exclusive large- R jet	8300000	2900000	140000	120000	520000	580000	1500000	210000	4900	5700	17000	62000	120000	140000	38000	100000	2700	120	210	330	530	1500
+ $60 < m_{\text{SD}} < 110 \text{ GeV}$	1100000	1200000	17000	72000	290000	480000	320000	87000	640	3300	9800	51000	22000	46000	31000	15000	1100	16	120	180	430	310
+ Sophon D_{bc} thres.	370	7600	100	6400	300	80	720	430	1.7	300	9.5	10	110	9.3	2.1	7.2	120	0.39	11	2.3	110	1.3
+ boosted-chn. classifier thres.	<2	25	<0.6	7.9	1.2	11	4.8	0.86	<0.9	<0.9	<0.9	0.86	<1.0	<1.0	<1.0	<1.0	15	<0.04	1.2	<0.04	14	0.10
Resolved channel																						
Pass 1 l trigger	250000000	1800000	—	—	—	—	1600000	—	—	—	—	2300000	—	—	18000	—	—	—	—			
+ ≥ 4 exclusive jets & $N_c = 1$	21000000	2100000	—	—	—	—	580000	—	—	—	—	200000	—	—	9600	—	—	—	—			
+ ≥ 3 b/c -tagged jets	210000	2300000	—	—	—	—	81000	—	—	—	—	3400	—	—	5100	—	—	—	—			
+ resolved-chn. classifier thres. A	<2	140	—	—	—	—	5.2	—	—	—	—	<2	—	—	63	—	—	—	—			
+ resolved-chn. classifier thres. B	<2	36	—	—	—	—	1.7	—	—	—	—	<2	—	—	26	—	—	—	—			

TABLE C2. Input objects features and vectors for the Particle Transformer event classifier in the boosted- and resolved-channel strategies.

Objects (N_{tokens})	Resolved channel: the triggered lepton (1), $p_{\text{T}}^{\text{miss}}$ (1), small- R jets exclusive to the triggered lepton (up to 6) Boosted channel: the triggered lepton (1), $p_{\text{T}}^{\text{miss}}$ (1), the W_{cand} large- R jet (1), small- R jets exclusive to the triggered lepton and W_{cand} (up to 5)
Object features	Resolved channel: $\log(p_{\text{T}})$, $\log(E)$, flag (is triggered lepton), flag (is $p_{\text{T}}^{\text{miss}}$), flag (is jet), flag (is B1-tagged jet), flag (is B2-tagged jet), flag (is C1-tagged jet), flag (is C2-tagged jet), flag (is N-tagged jet) Boosted channel: additionally including flag (is large- R jet)
Object vectors	Both channel: four-vectors p_i , used to compute pairwise variables: m_{ij}^2 , ΔR_{ij} , $z_{ij} = \frac{\min(p_{\text{T},i}, p_{\text{T},j})}{p_{\text{T},i} + p_{\text{T},j}}$, $k_{\text{T},ij} = \min(p_{\text{T},i}, p_{\text{T},j}) \Delta R_{ij}$

In estimating the precision of $|V_{cb}|$, it is important to account for the impact of b/c tagging efficiency uncertainties, which significantly limit the sensitivity of the resolved channel. In this study, we consider two additional scenarios for these uncertainties. Note that, in the default scenario, we assume that the uncertainties remain constant regardless of the integrated luminosity. This assumption is motivated by the CMS approach, where scale factors are measured separately for each data-taking year, leading to no reduction in statistical uncertainty despite increasing luminosity.

In the first scenario, we reduce all uncertainties by half. This approach allows us to systematically investigate the impact of uncertainty reduction on $|V_{cb}|$ precision. The results are summarized in Fig. C1 (left), showing the precision for the boosted channel, resolved channel, and their combination under this assumption. Notably, the sensitivity of the resolved channel is significantly improved, reaching a level comparable to the boosted channel at 3000 fb^{-1} . Comparing the combined results with the conventional one, the improvement in precision reduces from 30% to 15%. It is worth noting that under this assumption, we re-optimized the BDT thresholds for both the resolved and boosted channels. For the resolved channel, the change in threshold has a substantial impact on event yields, corresponding to option A in Table C1.

In the second scenario, we assume that the uncertainties from the default configuration, corresponding to 140 fb^{-1} , scale as $1/\sqrt{L}$ with luminosity L . This assumption is based on the premise that a unified tagging scale factor is derived for each experiment using the entire dataset. If the scale factor is dominated by statistical uncertainty, it would scale in this manner. Figure C1 (right) summarizes the $|V_{cb}|$ precision under this scaling assumption. The resolved channel shows better performance than the boosted channel. However, it is important to note that this scenario is likely overly optimistic. Even if a unified scale factor is derived from the full dataset, systematic effects would become more prominent, making the estimated 0.2 scaling at 3000 fb^{-1} overly optimistic compared to the default configuration.

[1] Y. S. Amhis *et al.* (Heavy Flavor Averaging Group (HFLAV)), Averages of b -hadron, c -hadron, and τ -lepton properties as of 2021, Phys. Rev. D **107**, 052008 (2023), arXiv:2206.07501 [hep-ex].

[2] S. Banerjee *et al.* (Heavy Flavor Averaging Group (HFLAV)), Averages of b -hadron, c -hadron, and τ -lepton properties as of 2023, (2024), arXiv:2411.18639 [hep-ex].
[3] S. Navas *et al.* (Particle Data Group), Review of particle

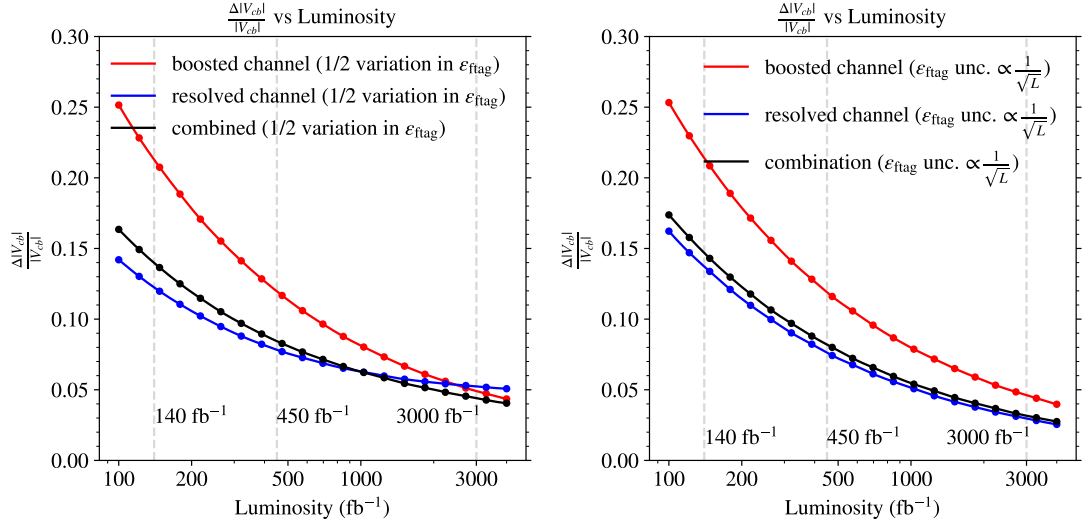


FIG. C1. The total fractional uncertainty of $|V_{cb}|$ obtained from the boosted and resolved channels, as well as their combination, presented under different luminosity conditions, is shown for two optimistic assumptions regarding the uncertainties in b/c flavor tagging efficiency. **Left:** Uncertainties are uniformly reduced by half across all luminosities. **Right:** Uncertainties scale with luminosity as $1/\sqrt{L}/140\text{fb}^{-1}$.

- physics, Phys. Rev. D **110**, 030001 (2024).
- [4] P. F. Harrison and V. E. Vladimirov, A Method to Determine $|V_{cb}|$ at the Weak Scale in Top Decays at the LHC, JHEP **01**, 191, arXiv:1810.09424 [hep-ph].
- [5] P. Azzi *et al.*, *Report from Working Group 1: Standard Model Physics at the HL-LHC and HE-LHC*, Tech. Rep. (2019) arXiv:1902.04070 [hep-ph].
- [6] H. Liang, L. Li, Y. Zhu, X. Shen, and M. Ruan, Measurement of CKM element $|V_{cb}|$ from W boson decays at the future Higgs factories, JHEP **12**, 071, arXiv:2406.01675 [hep-ph].
- [7] A. M. Sirunyan *et al.* (CMS), Inclusive search for a highly boosted Higgs boson decaying to a bottom quark-antiquark pair, Phys. Rev. Lett. **120**, 071802 (2018), arXiv:1709.05543 [hep-ex].
- [8] A. Tumasyan *et al.* (CMS), Search for nonresonant pair production of highly energetic Higgs bosons decaying to bottom quarks, Phys. Rev. Lett. **131**, 041803 (2023), arXiv:2205.06667 [hep-ex].
- [9] A. Tumasyan *et al.* (CMS), Search for Higgs boson decay to a charm quark-antiquark pair in proton-proton collisions at $\sqrt{s} = 13$ TeV, Phys. Rev. Lett. **131**, 061801 (2023), arXiv:2205.05550 [hep-ex].
- [10] A. Tumasyan *et al.* (CMS), Search for Higgs boson and observation of Z boson through their decay into a charm quark-antiquark pair in boosted topologies in proton-proton collisions at $\sqrt{s} = 13$ TeV, Phys. Rev. Lett. **131**, 041801 (2023), arXiv:2211.14181 [hep-ex].
- [11] A. M. Sirunyan *et al.* (CMS), Identification of heavy, energetic, hadronically decaying particles using machine-learning techniques, JINST **15**, P06005, arXiv:2004.08262 [hep-ex].
- [12] G. Aad *et al.* (ATLAS), Identification of boosted Higgs bosons decaying into b -quark pairs with the ATLAS detector at 13 TeV, Eur. Phys. J. C **79**, 836 (2019), arXiv:1906.11005 [hep-ex].
- [13] S. Choi and B. Kim, Measurement of the CKM matrix element $|V_{cb}|$ from top quark pair events at the LHC, J. Korean Phys. Soc. **78**, 1023 (2021).
- [14] C. Li *et al.*, Accelerating Resonance Searches via Signature-Oriented Pre-training, (2024), arXiv:2405.12972 [hep-ph].
- [15] CMS Collaboration, *Performance of heavy-flavour jet identification in boosted topologies in proton-proton collisions at $\sqrt{s} = 13$ TeV*, CMS Physics Analysis Summary CMS-PAS-BTV-22-001 (2022).
- [16] C. Li, *Modern deep learning for large- R jet tagging—algorithms, calibration methods, and applications in the CMS experiment*, Ph.D. thesis, Peking U., Beijing (2024), presented 24 May 2024.
- [17] M. Cacciari, G. P. Salam, and G. Soyez, The anti- k_T jet clustering algorithm, JHEP **04**, 063, arXiv:0802.1189 [hep-ex].
- [18] J. Alwall, R. Frederix, S. Frixione, V. Hirschi, F. Maltoni, O. Mattelaer, H. S. Shao, T. Stelzer, P. Torrielli, and M. Zaro, The automated computation of tree-level and next-to-leading order differential cross sections, and their matching to parton shower simulations, JHEP **07**, 079, arXiv:1405.0301 [hep-ph].
- [19] T. Sjöstrand, S. Ask, J. R. Christiansen, R. Corke, N. Desai, P. Ilten, S. Mrenna, S. Prestel, C. O. Rasmussen, and P. Z. Skands, An introduction to PYTHIA 8.2, Comput. Phys. Commun. **191**, 159 (2015), arXiv:1410.3012 [hep-ph].
- [20] J. de Favereau, C. Delaere, P. Demin, A. Giammanco, V. Lemaitre, A. Mertens, and M. Selvaggi (DELPHES 3), DELPHES 3, A modular framework for fast simulation of a generic collider experiment, JHEP **02**, 057, arXiv:1307.6346 [hep-ex].
- [21] G. Aad *et al.* (ATLAS), ATLAS flavour-tagging algorithms for the LHC Run 2 pp collision dataset, Eur. Phys. J. C **83**, 681 (2023), arXiv:2211.16345 [physics.data-an].
- [22] E. Bols, J. Kieseler, M. Verzetti, M. Stoye, and A. Stakia, Jet Flavour Classification Using DeepJet, JINST **15** (12),

- P12012, arXiv:2008.10519 [hep-ex].
- [23] H. Qu and L. Gouskos, ParticleNet: Jet Tagging via Particle Clouds, *Phys. Rev. D* **101**, 056019 (2020), arXiv:1902.08570 [hep-ph].
- [24] CMS Collaboration, *A unified approach for jet tagging in Run 3 at $\sqrt{s} = 13.6$ TeV in CMS*, CMS Detector Performance Summary CMS-DP-2024-066 (2024).
- [25] G. Aad *et al.* (ATLAS), Measurements of WH and ZH production with Higgs boson decays into bottom quarks and direct constraints on the charm Yukawa coupling in 13 TeV pp collisions with the ATLAS detector, (2024), arXiv:2410.19611 [hep-ex].
- [26] J. Alwall *et al.*, Comparative study of various algorithms for the merging of parton showers and matrix elements in hadronic collisions, *Eur. Phys. J. C* **53**, 473 (2008), arXiv:0706.2569 [hep-ph].
- [27] M. Czakon and A. Mitov, Top++: A program for the calculation of the top-pair cross-section at hadron colliders, *Comput. Phys. Commun.* **185**, 2930 (2014), arXiv:1112.5675 [hep-ph].
- [28] K. Melnikov and F. Petriello, Electroweak gauge boson production at hadron colliders through $O(\alpha_s^2)$, *Phys. Rev. D* **74**, 114017 (2006), arXiv:hep-ph/0609070.
- [29] N. Kidonakis, NNLL threshold resummation for top-pair and single-top production, *Phys. Part. Nucl.* **45**, 714 (2014), arXiv:1210.7813 [hep-ph].
- [30] T. Gehrmann, M. Grazzini, S. Kallweit, P. Maierhöfer, A. von Manteuffel, S. Pozzorini, D. Rathlev, and L. Tancredi, W^+W^- production at hadron colliders in next to next to leading order QCD, *Phys. Rev. Lett.* **113**, 212001 (2014), arXiv:1408.5243 [hep-ph].
- [31] R. D. Ball *et al.* (NNPDF), Parton distributions from high-precision collider data, *Eur. Phys. J. C* **77**, 663 (2017), arXiv:1706.00428 [hep-ph].
- [32] D. Bertolini, P. Harris, M. Low, and N. Tran, Pileup Per Particle Identification, *JHEP* **10**, 059, arXiv:1407.6013 [hep-ph].
- [33] M. Dasgupta, A. Fregoso, S. Marzani, and G. P. Salam, Towards an understanding of jet substructure, *JHEP* **09**, 029, arXiv:1307.0007 [hep-ph].
- [34] A. J. Larkoski, S. Marzani, G. Soyez, and J. Thaler, Soft Drop, *JHEP* **05**, 146, arXiv:1402.2657 [hep-ph].
- [35] H. Qu, C. Li, and S. Qian, Particle Transformer for jet tagging, in *Proceedings of the 39th International Conference on Machine Learning* (2022) pp. 18281–18292, arXiv:2202.03772 [hep-ph].
- [36] G. Aad *et al.* (ATLAS), ATLAS b-jet identification performance and efficiency measurement with $t\bar{t}$ events in pp collisions at $\sqrt{s} = 13$ TeV, *Eur. Phys. J. C* **79**, 970 (2019), arXiv:1907.05120 [hep-ex].
- [37] G. Aad *et al.* (ATLAS), Measurement of the c-jet mistagging efficiency in $t\bar{t}$ events using pp collision data at $\sqrt{s} = 13$ TeV collected with the ATLAS detector, *Eur. Phys. J. C* **82**, 95 (2022), arXiv:2109.10627 [hep-ex].
- [38] G. Aad *et al.* (ATLAS), Calibration of the light-flavour jet mistagging efficiency of the b-tagging algorithms with Z+jets events using 139 fb $^{-1}$ of ATLAS proton–proton collision data at $\sqrt{s} = 13$ TeV, *Eur. Phys. J. C* **83**, 728 (2023), arXiv:2301.06319 [hep-ex].
- [39] CMS Collaboration, *Performance summary of AK4 jet b tagging with data from proton-proton collisions at 13 TeV with the CMS detector*, CMS Detector Performance Summary CMS-DP-2023-005 (2023).
- [40] CMS Collaboration, *Performance summary of AK4 jet charm tagging with the CMS Run2 Legacy dataset*, CMS Detector Performance Summary CMS-DP-2023-006 (2023).
- [41] B. A. Roberts, *Progress towards the first measurement of the V_{cb} element of the CKM matrix in semi-leptonic $t\bar{t}$ decays*, Ph.D. thesis, Warwick U. (2022), presented 2022.